Thulium fiber lasers with longitudinally modified concentration

Bára Švejkarová[1,2], Martin Grábner[1], Jan Aubrecht[1], Richard Švejkar[3], Jan Pokorný[1,2], Michal Kamrádek[1], Ondřej Podrazký[1], Ivan Kašík[1], Pavel Honzátko[1], Andrew Clarkson[3], and Pavel Peterka[1]

[1]*Institute of Photonics and Electronics, Chaberská 1014/57, 182 00 Prague, Czech Republic*

[2]*Faculty of Nuclear Sciences and Physical Engineering, Czech Technical University in Prague, Břehová 7, 115 19 Prague, Czech Republic*

[3]*Optoelectronics Research Centre, University of Southampton, University Rd., SO17 1BJ Southampton, United Kingdom*

Abstract

High-power fiber lasers generate local heat load extremes during their operation, which increase the fiber temperature and lead to adverse thermal effects, such as transverse mode instability or cladding/coating thermal damage. The local temperature extremes are usually located near the end of a fiber where the pump power is delivered. In this paper, longitudinally inhomogeneous doping concentration profiles are applied to reduce the heat load extremes. Utilizing a new degree of freedom, it is shown by both simulations and measurements that maximal temperature along the fiber can be effectively decreased by using active fibers with an increasing concentration profile in the direction of pumping power. The concept is studied by a comprehensive numerical model that considers temperature-dependent parameters and is also demonstrated by measurement on an in-house built thulium-doped fiber laser formed by spliced sections with different concentrations. The output power of 54 W with the slope efficiency exceeding 62 % was reached.

Keywords: fiber laser; thulium; heat load; temperature; concentration profile

1. Introduction

The performance of high-power fiber lasers is affected by thermal effects of different kinds such as transverse mode instability or cladding/coating thermal damage. The thermal management of high-power fiber lasers is thus an important part of their design, especially in cases with large quantum defect such as in thulium-doped fiber lasers (TDFL)[1–3] operating around 2 μm and pumped at 790 nm. Since the heat load and thus temperature have their maximum usually near a fiber end where the pump power is delivered, this location is critical in terms of thermal management.

Heat load maximum appears due to the highest pump absorption that is proportional to active ion concentration. Therefore one possibility to reduce a heat load maximum is to decrease concentration and increase fiber length proportionally to keep the their product constant. Such a method has its limitations in thulium-doped fibers (TDF) because a low concentration of Tm^{3+} ions leads to a less efficient two-for-one process that is known to enhance slope efficiency. Spatially dependent concentration in a fiber cross-section can reduce the heat load while maintaining high efficiency but there is yet another degree of freedom, not investigated so far, that can be utilized to modify heat load distribution along the active fiber. It is demonstrated here that the longitudinally inhomogeneous profile of concentration can serve to decrease extremes of heat load and temperature.

Several approaches were studied for the thermal management of solid-state and fiber lasers. Primarily, efficient cooling methods were sought that can extract generated heat out of the active fiber to the fiber surrounding. For example, cooling efficiency in different geometries was analyzed[4,5]. Different materials of cladding and coating including metal clad[6] were proposed for thermal management of active fibers at the kW level. The general conclusion of these studies is that the cooling medium is to be placed as close to the fiber core as possible avoiding any intermediate materials with low thermal conductivity. The performance of this practical strategy is limited by an outer fiber diameter that it is often large (400 μm) in high-power double-clad fibers.

An all optical approach of thermal management based on radiation cooling by anti-Stokes fluorescence was

---

proposed for solid state lasers[7]. The method that was also studied in the context of Yb-doped fiber lasers[8–12] can in principle achieve nearly zero heat generation by ensuring radiation-balanced lasing when time-averaged absorbed power density equals to the radiated power density due to stimulated and spontaneous emission. This approach can have a great potential in cases where its application conditions are met, i.e. for low quantum defects and $\nu_s < \nu_p < \nu_f$ where ν_s, ν_p, ν_f are lasing, pump, and average spontaneous emission (fluorescence) frequencies.

Spatially dependent rare-earth dopant concentration was found fruitful in high-power solid state (crystal) lasers. A multi-slab Yb^{3+}:YAG laser with different concentration in each slab were proposed[13,14] as a way to ensure uniform heat load in each slab. The concept was studied numerically by a three-dimensional ray-tracing code[15] and by solving propagation equations[16]. It was optimized in the record-breaking solid-state laser Bivoj[17]. Segmented Ho^{3+}:YAG crystal lasers were studied experimentally too[18]. Gradient-doped crystals were investigated to increase pumping efficiency[19] and demonstrated to limit the temperature extreme[20].

The concept of spatially dependent dopant concentration in active optical fibers has been investigated so far merely only in the context of fiber cross-section in-homogeneity, intended, or parasitic. Various methods were proposed to measure concentration distribution in fiber cross-section[21–23]. Functional active fibers adopting MCVD and other doping techniques to tailor the transverse doping profile, e.g. confined-doped fibers can exhibit benefits such as higher overlap of the mode field with active area improving the beam quality[24]. Ring-shaped doping profiles were shown to reduce the gain of amplified spontaneous emission and to shift the gain peak to the shorter wavelengths, e.g. nested ring Tm-doped fiber provided lasing at 1907 nm with reduced thermal load and without parasitic lasing at longer wavelengths[25].

To the best of our knowledge, the concept of active fibers with longitudinally inhomogeneous concentration has not been investigated so far. It is motivated in the next section where the simplest model is applied to show how the heat load maximum is reduced when a suitable concentration profile is considered.

2. Search for maximally flat heat load

Let us consider the simplified model of pump power absorption with a constant pump absorption coefficient α_p [1/m]. From the propagation equation for pump power P_p:

$$\frac{dP_p(z)}{dz} = -P_p(z)\alpha_p \qquad (1)$$

it follows that pump power decreases along the fiber (z coordinate) as: $P_p(z) = P_p(0)\exp(-\alpha_p z)$. The pump

absorption is proportional to concentration N_t as: $\alpha_p = \sigma_{pa}\bar{N}_0 N_t \Gamma_p$ where σ_{pa} is the absorption cross-section at the pump wavelength, $\bar{N}_0 = N_0/N_t$ is relative ground level population and Γ_p is pump field overlap with the doped area. If a *constant* power conversion efficiency between the signal power P_s and the pump power is assumed $\eta = dP_s/dP_p$ and assuming that all pump not converted to signal is converted to heat, the heat load per unit length is

$$
\begin{aligned}
Q(z) &= (1-\eta)(-dP_p/dz) &\qquad (2)\\
&= (1-\eta)P_p(0)\alpha_p \exp(-\alpha_p z) &\qquad (3)
\end{aligned}
$$

and reaches its maximum at $z = 0$.

Our task is to find the concentration profile $N_t(z)$ that leads to a maximally flat heat load profile along the fiber of a length L. This is achieved by assuming pump dependence in the form: $P_p(z) = P_p(0)(1 - z/L)$. Its derivative $dP_p/dz = -P_p(0)/L$ is also equal to the right hand side of (1) where the absorption coefficient $\alpha_p(z)$ is now considered to be a function of z. Therefore

$$\alpha_p(z) = \frac{P_p(0)}{P_p(z)L} = \frac{1}{L-z} \qquad (4)$$

and concentration is $N_t(z) = \alpha_p(z)/(\bar{N}_0 \sigma_{pa}\Gamma_p)$. The heat load with this concentration profile is z-independent, i.e.: $Q_l(z) = (1-\eta)P_p(0)/L$. Note that $\alpha_p(0) = 1/L$ and $\alpha_p(L)$ diverges in formula (4). The situation is shown in the example in Fig. 1 where power and heat load profiles are compared for constant concentration and for concentration profile using (4). The heat load maximum $Q(z=0) = 0.38$ W/m is reduced to $Q(z) = 0.1$ W/m if the inhomogeneous profile is applied.
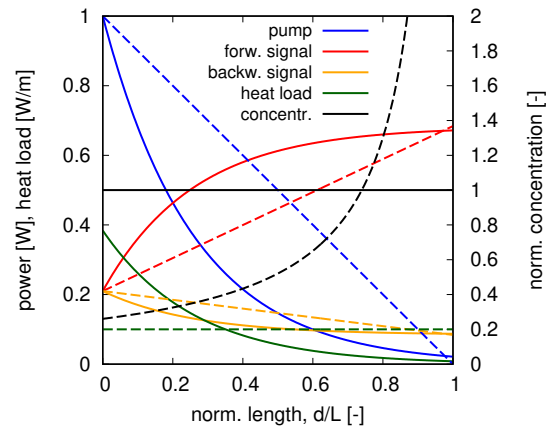

Figure 1. Power and heat load profiles along the active fiber in an oscillator configuration with constant concentration (solid lines) and with an inhomogeneous concentration profile $N_t(z)$ for maximally flat heat load (dashed lines). Parameters: $L = 4$ m, $\eta = 0.6$, $\sigma_{pa} = 8 \times 10^{-25}$ m^2, $N_t = 2.4 \times 10^{26}$ m^{-3}, $\Gamma_p = 0.005$, $N_0 \sim 1$.

While the above example demonstrates the concept, the theoretical profile (4) cannot be realized even in principle

because of its divergence at $z = L$. Furthermore, the simplified model is not adequate to describe all important fiber laser features. Therefore more realistic concentration profiles will be analyzed using a comprehensive numerical model[26].

3. Numerical simulation

3.1. Numerical model

The comprehensive numerical model is based on the solution of laser rate equations together with wavelength-resolved propagation equations for power spectral density[26]. It takes into account a lot of physically relevant effects that are important for realistic modeling of high-power fiber lasers like the amplified spontaneous emission, fiber temperature changes due to self-heating[26] based on the analytic model for a temperature radial profile in the fiber[27], temperature-dependent absorption and emission cross-section spectra[28,29], intrinsic fiber attenuation, cross-relaxation dependence on concentration.

3.2. Model parameters

High-power TDFL parameters applied in the numerical model are essentially the same as reported in[26]. While the majority of the parameters including e.g. spectroscopic parameters of Tm^{3+} ions in silica are known with sufficient accuracy, the parameters determining the exact relationship between fiber temperature and the heat load depends on fiber cooling efficiency provided by a cooling system and thus they are problem-specific. In order to demonstrate the concept, the analytical model[27] for temperature radial distribution in a layered medium is used with the following set of parameters: doped core with a radius $a_1 = 10\ \mu$m, silica cladding $a_2 = 200\ \mu$m, polymer coating $a_3 = 300\ \mu$m, thermally conducting paste $a_4 = 500\ \mu$m, aluminum heat sink $a_5 = 501\ \mu$m. Thermal conductivity values in different layers are $k_1 = k_2 = 1.38$, $k_3 = 0.18$, $k_4 = 0.15$, $k_5 = 238$ Wm^{-1}K^{-1}. Background temperature is set to 23 °C. Note that the analytical model uses cylindrical layers; in section 4.2 we show, for comparison, the temperature distribution for real geometry calculated by a numerical model, see the inset in Fig. 9.

3.3. Concentration profiles

Several concentration longitudinal profiles were selected to be analyzed and compared with a constant concentration case. The *linear* profile is defined as:

$$N_t(\zeta) = \bar{N}_t(a\zeta + b), \quad a = 2(1-b) \quad (5)$$

where $\zeta = z/L$ is the relative longitudinal coordinate, a, b are mutually dependent parameters and $\bar{N}_t$ is the average concentration along the fiber $\bar{N}_t = (1/L)\int_0^L N_t(z)dz$. The

step profile is defined as:

$$N_t(\zeta) = \bar{N}_t a_i, \quad \zeta_i \leq \zeta < \zeta_{i+1}, \quad i = 1, 2 \ldots \quad (6)$$

where a_i is the relative concentration in the i-th section and ζ_i is the relative coordinate of the i-th section beginning. The *gauss* profile is defined as:

$$N_t(\zeta) = \bar{N}_t C \exp\left(-\frac{(\zeta - \mu)^2}{2\sigma^2}\right) \quad (7)$$

where μ and σ are the mean value and standard deviation of the gauss profile and C is a normalization constant. The *tanh* profile is defined as:

$$N_t(\zeta) = \bar{N}_t\left[a + (b-a)\frac{1}{2}(1 + \tanh(\sigma(\zeta - \mu)))\right] \quad (8)$$

where a and b are minimum and maximum relative concentration and μ, σ are shifting and scaling parameters. The *inverse distance* profile is defined as modification of (4) as:

$$N_t(\zeta) = \frac{1}{\sigma_{pa}\Gamma_p}\frac{1}{L' - L'\zeta'} \quad (9)$$

$$\zeta' = \frac{\zeta}{(1 + |\zeta|^p)^{1/p}} \quad (10)$$

$$p = \frac{-\ln 2}{\ln(1 - 1/(N_{tm}\sigma_{pa}\Gamma_p L'))} \quad (11)$$

where $L' = cL$, such that $c \leq 1$, is a shorter-than-fiber-length distance and N_{tm} is a maximal concentration parameter.

3.4. Temperature vs concentration profiles

In order to demonstrate the influence of longitudinally inhomogeneous concentration on power and temperature distribution along the active fiber, the cladding-pumped TDFL example is analyzed.

In the analyzed example, the following parameters are assumed: fiber length $L = 7$ m, core diameter $d_c = 20\ \mu$m, cladding diameter $d_{cl} = 400\ \mu$m, coating diameter $d_{ct} = 600\ \mu$m (note that $d_c = 2a_1$, $d_{cl} = 2a_2$, $d_{ct} = 2a_3$), numerical aperture NA=0.3, average concentration $\bar{N}_t = 2.4 \times 10^{26}$ m^{-3}, pump wavelength $\lambda_p = 790$ nm, signal wavelength $\lambda_s = 2000$ nm, reflectivities $R_1 = 0.99$, $R_2 = 0.036$, signal and pump overlap factors $\Gamma_s = 0.90$, $\Gamma_p = 0.0025$. The temperature-dependent cross-section spectra (the Cryo variant[29]) are applied.

Figure 2 compares six longitudinal profiles of concentration $N_t(z)$ with the *same average concentration* $\bar{N}_t = 2.4 \times 10^{26}$ m^{-3}. The constant concentration profile (Fig. 2a leads to the maximum core temperature of 127.7 °C that is located near the beginning of a fiber. The maximum of forward propagating signal power $P_f(\lambda_s)$ is 592.1 W. Assuming the linear profile of concentration according to (5) with $b = 0.7$, see Fig. 2b, the maximum core temperature decreased
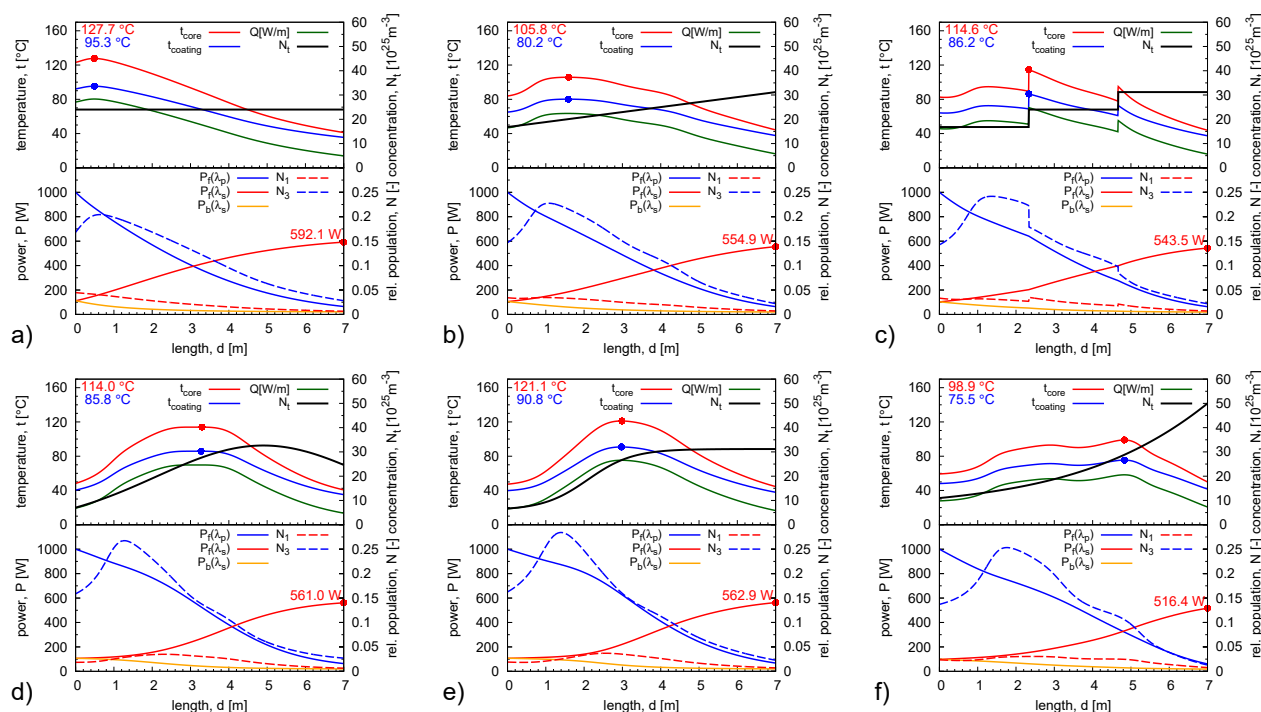
Figure 2. Power and temperature distribution along TDFL (pump power $P_p = 1000$ W), a) constant concentration, b) linear profile, c) step profile, d) gauss profile, e) tanh profile, f) inverse distance profile. All profiles with the same average concentration $\bar{N}_t = 2.4 \times 10^{26}$ m^{-3} (~ 10900 mol ppm). Notes: numerical values of heat load Q [W/m] are on temperature axis; $P_f(\lambda_p)$ forward propagating pump power, $P_f(\lambda_s)$ forward propagating signal power, $P_b(\lambda_s)$ backward propagating signal power.

to 105.8 °C and its position shifted inside the fiber. The maximal signal power also decreased to 554.9 W. Assuming the step-wise concentration profile according to (6) with parameters: $\zeta_1 = 0$, $\zeta_2 = 0.33$, $\zeta_3 = 0.66$, $a_1 = 0.7$, $a_2 = 1$, $a_3 = 1.3$, see Fig. 2c, the maximal temperature drops to 114.6 °C but the discontinuities of temperature appear at the positions of abrupt changes in the concentration profile. Assuming the gauss profile according to (7) with parameters: $\mu = 0.7$, $\sigma = 0.4$, see Fig. 2d, the maximal temperature is 114 °C with a maximal signal power of 561 W. Assuming the tanh profile according to (8) with parameters: $a = 0.25$, $b = 1.3$, $\mu = 0.3$, $\sigma = 6$, see (Fig. 2e), the maximal core temperature is 121.1 °C with a maximal signal power of 562.9 W. The inverse distance profile according to (11) with parameters: $c = 0.55$, $N_{tm} = 5 \times 10^{26}$, see Fig. 2f, exhibits the greatest drop of maximum temperature to 98.9 °C but clearly at the expense of the output power since maximal signal power is $P_f(\lambda_s) = 516.4$ W. Note that laser output power is $P_{sout} = P_f(\lambda_s, z = L)(1 - R_2)$.

The relation between laser output signal power and maximum core temperature along the fiber is depicted in Fig. 3 where the profiles with the same average concentration are compared. The output signal power values were achieved by applying pump power from 200 W to 2000 W with 100 W steps, see dots. Clearly, maximal fiber temperature limits the achievable output power or in other words the particular output power leads to different fiber temperature with

different concentration profiles. Note that the temperature differences are less pronounced in the case of coating temperature.
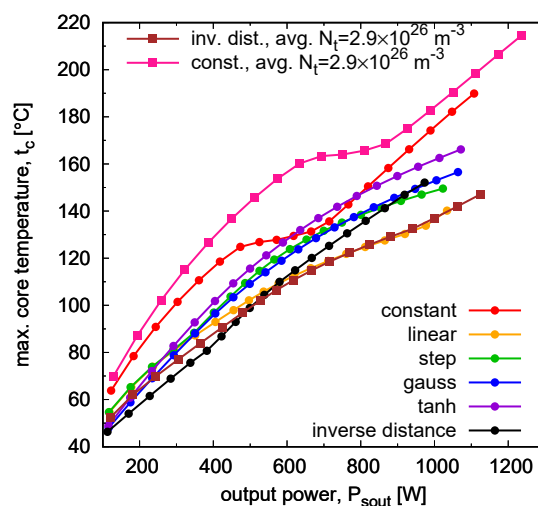

Figure 3. Maximal core temperature vs laser output signal power (for pump power $P_p = (200:100:2000)$ W) for different concentration profiles with the same average concentration $\bar{N}_t = 2.4 \times 10^{26}$ m^{-3} (~ 10900 mol ppm) (circles) and for inverse distance and constant profiles with $\bar{N}_t = 2.9 \times 10^{26}$ m^{-3} (~ 13100 mol ppm) (squares).

It is evident from the presented examples and Fig. 3

that reducing maximal temperature is achieved only at the expense of efficiency (i.e. the ratio of output power to pump power). However, one can achieve the same output power with the same pumping power and still significantly reduce a temperature by using a higher average concentration. The inverse distance profile with parameters $c = 0.4$, $N_{tm} = 5 \times 10^{26}$ and average concentration $\bar{N}_t = 2.9 \times 10^{26}$ m^{-3} is analyzed in Fig. 4. The same maximal signal power is achieved as in the case of constant concentration $\bar{N}_t = 2.4 \times 10^{26}$ m^{-3} but here the maximal core temperature is reduced to 106.4 °C which is more than 20 °C less than in the case of constant concentration (with the same output signal power). This inverse distance profile with higher average concentration is also shown in Fig. 3, see square dots, to achieve a significant reduction of temperature with the same or slightly better efficiency in comparison with the case of constant profile.
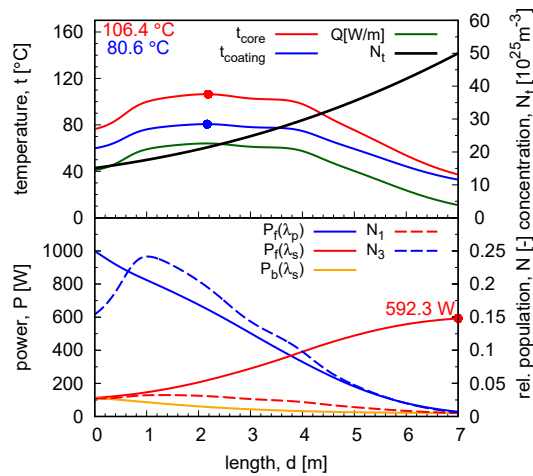

Figure 4. Power and temperature distribution along TDFL (pump power $P_p = 1000$ W), inverse distance profile with the average concentration $\bar{N}_t = 2.9 \times 10^{26}$ m^{-3} (~ 13100 mol ppm)

Note, that a constant concentration profile with an increased average concentration would provide even higher output power but also significantly higher maximal heat load and temperature. Therefore, using a suitable inhomogeneous profile one can set a better trade-off between power and temperature, or in other words, the higher output power can be achieved under the requirement that prescribed maximum temperature limit is not to be exceeded.

For example, let us assume that the coating temperature t_{ct} has to be kept lower than 81 °C. Taking this limit into account, the maximum signal power 574.4 W can be achieved with maximum core temperature $t_c = 106.9$ °C, the maximum coating temperature $t_{ct} = 80.9$ °C for lower *constant* concentration $N_t = 2.05 \times 10^{26}$ m^{-3} and increased fiber length $L = 12$ m. Note that output signal power is lower than in Fig. 4 where the same temperature limits are fulfilled by using an inverse distance profile on a 7 m long

fiber.

The numerical model of fiber laser respects non-uniform pump absorption due to non-uniform population inversion along the fiber but assumes a homogeneous overlap factor of the pump field with the doped area. However, simulations of electromagnetic field propagation[30] in double-clad active fibers show that the overlap and resulting pump absorption profile are also dependent on the spatial distribution of the excitation field and on the cladding geometry.

4. Experiment

A practical demonstration of longitudinally inhomogeneous concentration in TDFL was performed by multi-segmented active fibers with varying configurations.

4.1. Methodology

An in-house prepared double-clad fiber (SG1647) with inhomogeneous thulium concentration was used for the experiments. That allowed the selection of various sections with different concentrations with a minimal variation in the refractive index profile, thus reducing the splice losses between different parts of the fiber. However, it is essential to clarify that this inhomogeneity was not localized in the short fiber segments. The fiber was processed to a quasi-octagonal shape with core, pedestal, and cladding (flat to flat) dimensions of 12, 31, and 132 μm, respectively. During the experiment, the fiber was placed on the aluminum plate and fixed using a Kapton tape on several spots. This arrangement allowed for optimal conditions to observe heat distribution.

In the initial stage, the individual segments with a Tm^{3+} concentration of 6900 (A), 11800 (B), 13700 (C), and 16000 (D) molar ppm were measured separately. The concentration was calculated based on the measured cladding absorption and the cladding/core radius ratio. In a 100%-4% setup, shown in Fig. 5, the resonator was formed by high reflectivity (HR) fiber Bragg grating (FBG), centered around 1940 nm (AFR/TeraXion), along with a perpendicularly cleaved end. The pump was provided by a laser diode (LD) operating at 792 nm (Aerodiode/BWT) protected from 2 μm radiation by fiber with high OH concentration (Hi OH, Thorlabs FG105UCA). Individual segments were measured up to a pump power of 30 W. A passive fiber (Nufern SM-GDF 10/130 μm) was utilized to minimize mode-field diameter mismatch between the active fiber and the various FBGs. The unabsorbed pump power was separated by a silicon filter or dichroic mirror. Using cut-back measurement, the
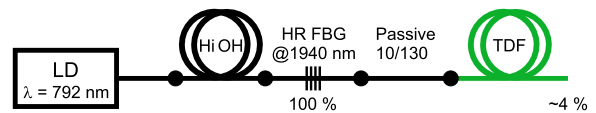

Figure 5. Experimental setup of the TDFL.

maximal slope efficiency with respect to pump power was determined.

In the next step, two 2-segmented lasers were prepared to compare segmented and uniformly doped active fibers in the resonator. Both had the same fiber length and similar average concentration and they contained a splice in between to minimize their influence. These splices were created using an optimized program on the splicer (Fitel S185) providing the loss estimation based on image analysis as well. Additionally, we tested 3- and 4-segmented lasers to demonstrate the character of the step-profile laser. All TDFLs were tested using the same setup as for the individual segments. During the characterization, the spectra were measured with an optical spectrum analyzer (Yokogawa AQ6375), and the surface temperature was monitored using a thermal camera (Micro-epsilon TIM40).

4.2. Results

Table 1 summarizes the slope efficiencies for individual segments. According to these results, segmented TDFLs

Table 1. Slope efficiency for individual segments pumped up to 30 W.

Fiber label	A	B	C	D
Concentration [mol ppm]	6900	11800	13700	16000
Fiber length [m]	4.0	3.0	2.5	3.0
Slope efficiency [%]	58.2	64.7	65.8	66.2
Threshold [W]	1.68	2.16	2.12	2.35

were formed by splicing together individual segments. The particular compositions of the segmented TDFLs are listed in Table 2.

Table 2. Composition of formed segmented TDFLs, all units are in meters.

Fiber [m]	A	B	C	D
2-seg TDFL	0.7	–	–	2.1
2-seg uniform TDFL	–	–	0.8+2.0	–
3-seg TDFL	0.5	–	1.1	2.2
4-seg TDFL	0.4	0.4	0.8	1.7

Figure 6 shows the performance of 2-segmented TDFLs. The segmented laser's slope efficiency was 65.3 %, consistent with the uniformly doped one. However the 2-seg uniform TDFL did not last out the pump power above 40 W. The thermal camera image in Fig. 7 illustrates well the fundamental principles of multi-segment laser operation. The temperature label indicates the highest value in the marked area. At the same pump power, the heat distribution along the segmented fiber was more even, allowing the fiber to handle higher pump powers.

Additional segments were added to the laser configuration for further experiments. The 3-segmented laser demonstrated performance reaching a slope efficiency of 62 %, as shown in Fig. 8a. The thermal camera image in Fig. 8b indicates a
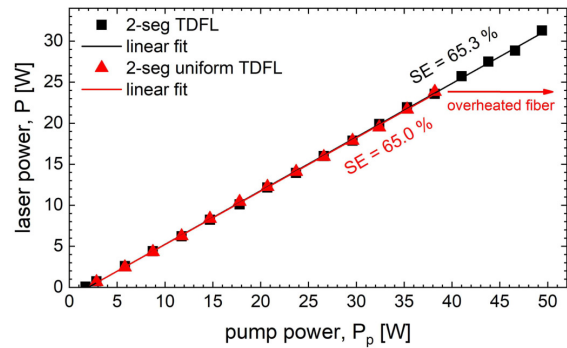
Figure 6. Laser performance comparison of 2-segmented and uniformly doped fiber. Both TDFLs have similar average Tm concentration and fiber length.
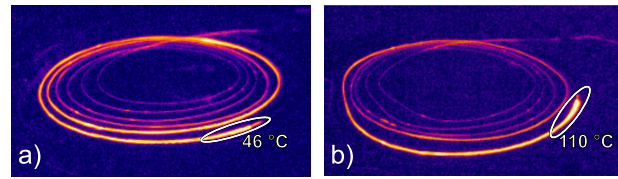
Figure 7. Thermal image of a) 2-seg TDFL b) 2-seg uniform TDFL under the same pump powers. The temperature of 110 °C was reached just before the splice failure.

notably improved heat distribution. The image also shows that the splice between the first and second segments (S1-S2) was warmer than the splice where the pump power enters the first segment of the active fiber (FBG-S1). This observation suggests that the lengths and concentrations of the individual active fibers can be designed more effectively.
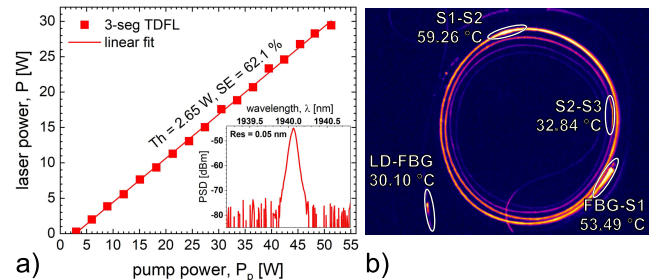
Figure 8. a) The performance of 3-segmented TDFL, b) thermal camera image at a pump power of 28 W.

The temperature at the outer coating along the fiber determined from the thermal camera image is compared with the simulated fiber temperature in Fig. 9. The temperature was calculated from the heat load Q using the analytical model[27] calibrated by Comsol heat transfer simulations of an active fiber placed on the cooled plate, see the inset of Fig. 9. The temperature peaks were modeled by introducing 'splice losses' L_s = 0.02, 0.025, and 0.012 dB/cm at locations z = 0, 55, and 162 cm along the fiber, based on the experimental observations. It is evident that in the first
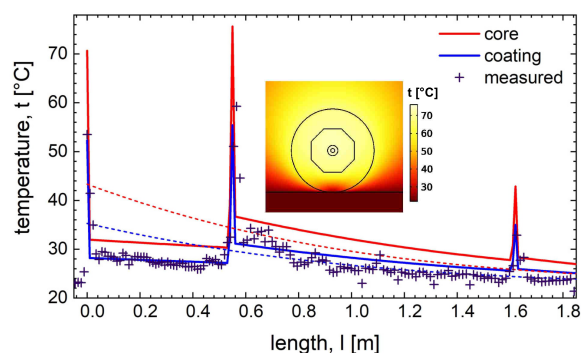
Figure 9. Measured (crosses) and simulated (lines) fiber temperature of 3-segmented TDFL at a pump power of 28 W vs uniform fiber with the same average concentration (dashed lines). Inset: Simulated temperature distribution of active fiber laying on a cooling desk under core heat load $Q = 20$ W/m.

50 cm of the fiber where $Q(z) \sim 4$ W/m, the temperature was significantly lower compared with the case of uniform fiber with the same average concentration (see dashed lines).

Based on these findings, an attempt was made to further improve laser performance by integrating a fourth segment. In particular, the segment B was placed at the second position to achieve a more gradual increase of Tm ion concentration while maintaining approximately the same resonator length and same total averaged concentration. It reduced the temperature of the splice S1-S2 (compare Figs. 8 and 10) and the segment C could be shortened, as the last splice was not at higher risk of heat damage. The laser exhibited a stable output power of 54 W and even greater improvements in slope efficiency exceeding 64 % with the pump power up to 30 W and 62 % for high power test, shown in Fig. 10. Furthermore, the threshold was lowered
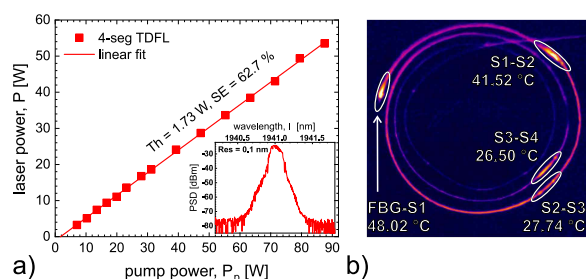

Figure 10. a) The performance of 4-segmented fiber laser, b) thermal camera image at a pump power of 33 W.

compared to individual segments with higher concentrations. See Fig. 11 for the summary of slope efficiency and threshold power.

5. Conclusion

Segmented active fibers were utilized to distribute the heat load along the fiber more effectively during laser operation. A comparison between the 2-segmented fiber
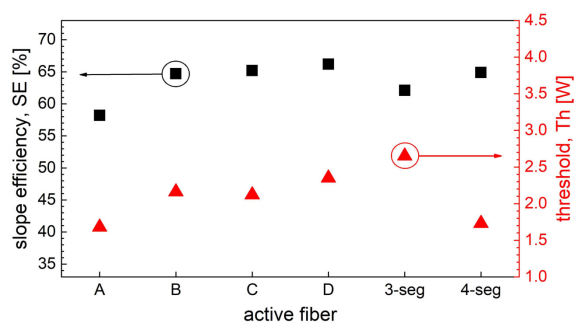

Figure 11. Summary of the measurements at the pump power up to 30 W.

and the uniformly doped fiber with the same length and average concentration demonstrated that the segmented design allows for better heat distribution, enabling it to withstand higher pump powers and maintain good efficiency at the same time.

The output power of 30 W and 54 W was achieved for the 3-segmented and 4-segmented TDFL, respectively. Both lasers exceed the slope efficiency of 62 %, comparable with individual segments, although they contain splices between the active fibers. This could be improved by using a single fiber with a concentration gradient, which is challenging to achieve with the current state of technology.

Fiber lasers with longitudinally segmented fibers provide promising solutions for integrating highly doped TDFs with an efficient 2-for-1 process into the laser while minimizing thermally induced damage, leading to efficient high-power lasers.

References

1. M. Wang, Y. Huang, Z. Song, J. Wei, J. Pei, and S. Ruan. Two-micron all-fiberized passively mode-locked fiber lasers with high-energy nanosecond pulse, High Power Laser Sci. Eng. **8**, e14 (2020). DOI:10.1017/hpl.2020.7.

2. Y. Xiao, X. Xiao, L. Liu, and H. Guo. Gain-switched watt-level thulium-doped fiber laser and amplifier operating at 1.7 μm, High Power Laser Sci. Eng. **10**, e40 (2022). DOI:10.1017/hpl.2022.33.

3. B. Ren, C. Li, T. Wang, K. Guo, J. Wu, and P. Zhou. Thulium-doped all-pm fiber chirped pulse amplifier delivering 314 W average power, High Power Laser Sci. Eng. **11**, e73 (2023). DOI:10.1017/hpl.2023.68.

4. M.-A. Lapointe, S. Chatigny, M. Piché, M. Cain-Skaff, and J.-N. Maran. Thermal effects in high-power

CW fiber lasers, In *Fiber Lasers VI: Technology, Systems, and Applications*, volume 7195, pp. 430–440, (SPIE2009). DOI:10.1117/12.809021.

5. Y. Fan, B. He, J. Z. . J. Zheng, S. Dai, C. Zhao, Y. Wei, and Q. Lou. Efficient heat transfer in high-power fiber lasers, Chinese Opt. Lett. **10**, 111401 (2012). DOI:10.3788/col201210.111401.

6. J. M. Daniel, N. Simakov, A. Hemming, W. A. Clarkson, and J. Haub. Metal clad active fibres for power scaling and thermal management at kW power levels, Opt. Express **24**, 18592 (2016). DOI:10.1364/OE.24.018592.

7. S. R. Bowman. Lasers without internal heat generation, IEEE J. Quantum Electron. **35**, 115 (1999). DOI:10.1109/3.737628.

8. G. Nemova and R. Kashyap. Athermal continuous-wave fiber amplifier, Opt. Commun. **282**, 2571 (2009). DOI:10.1016/J.OPTCOM.2009.03.038.

9. G. Nemova. Brief review of recent developments in fiber lasers, Appl. Sci. **14**, 2323 (2024). DOI:10.3390/app14062323.

10. J. Ballato, P. D. Dragic, and M. J. Digonnet. Prospects and challenges for all-optical thermal management of fiber lasers, J. Phys. D: Appl. Phys. **57**, 162001 (2024). DOI:10.1088/1361-6463/ad1ddc.

11. J. Knall, P.-B. Vigneron, M. Engholm, P. D. Dragic, N. Yu, J. Ballato, M. Bernier, and M. J. Digonnet. Laser cooling in a silica optical fiber at atmospheric pressure, Opt. Lett. **45**, 1092 (2020). DOI:10.1364/OL.384658.

12. N. Yu, J. Ballato, M. J. Digonnet, and P. D. Dragic. Optically managing thermal energy in high-power Yb-doped fiber lasers and amplifiers: a brief review, Curr. Opt. Photonics **6**, 521 (2022). DOI:10.3807/COPP.2022.6.6.521.

13. P. D. Mason, K. Ertel, S. Banerjee, P. J. Phillips, C. Hernandez-Gomez, and J. L. Collier. Optimised design for a 1 kJ diode-pumped solid-state laser system, In *Diode-Pumped High Energy and High Power Lasers; ELI: Ultrarelativistic Laser-Matter Interactions and Petawatt Photonics; and HiPER: the European Pathway to Laser Energy*, volume 8080, pp. 268–276, (SPIE2011). DOI:10.1117/12.892317.

14. S. Banerjee, K. Ertel, P. D. Mason, P. J. Phillips, M. Siebold, M. Loeser, C. Hernandez-Gomez, and J. L. Collier. High-efficiency 10 J diode pumped cryogenic gas cooled Yb:YAG multislab amplifier, Opt. Lett. **37**, 2175 (2012). DOI:10.1364/OL.37.002175.

15. M. Sawicka, M. Divoky, J. Novak, A. Lucianetti, B. Rus, and T. Mocek. Modeling of amplified spontaneous emission, heat deposition, and energy extraction in cryogenically cooled multislab Yb^{3+}:YAG laser amplifier for the HiLASE project, JOSA B **29**, 1270 (2012). DOI:10.1364/JOSAB.29.001270.

16. M. Li, X. Zhang, X. Yan, X. Cui, Z. Wang, K. Xiao, X. Jiang, J. Zheng, W. Wang, and M. Li. Theoretical analysis of uniform longitudinal gain for a double-end-pumped Yb:YAG multi-slab pulsed amplifier, Opt. Commun. **393**, 199 (2017). DOI:10.1016/j.optcom.2017.02.019.

17. M. Divoký, J. Pilař, M. Hanuš, P. Navrátil, O. Denk, P. Severová, P. Mason, T. Butcher, S. Banerjee, M. De Vido, et al. 150 J DPSSL operating at 1.5 kW level, Opt. Lett. **46**, 5771 (2021). DOI:10.1364/OL.444902.

18. K. Goth, M. Rupp, M. Griesbeck, M. Eitner, M. Eichhorn, and C. Kieleck. Investigation of high-power Ho^{3+}:YAG lasers with homogeneous and segmented crystals, In *Laser Congress 2023 (ASSL, LAC)*, p. AM6A.7, (Optica Publishing Group2023). DOI:10.1364/ASSL.2023.AM6A.7.

19. E. Stroganova, V. Galutskiy, D. Tkachev, N. Nalbantov, A. Tsema, and N. Yakovenko. Increasing pumping efficiency by using gradient-doped laser crystals, Opt. Spectrosc. **117**, 984 (2014). DOI:10.1134/S0030400X14120236.

20. M. Wei, T. Cheng, R. Dou, Q. Zhang, and H. Jiang. Superior performance of a 2 kHz pulse Nd:YAG laser based on a gradient-doped crystal, Photonics Res. **9**, 1191 (2021). DOI:10.1364/PRJ.424989.

21. A. Yablon. Measuring the spatial distribution of rare-earth dopants in high-power optical fibers, In *Fiber Lasers VIII: Technology, Systems, and Applications*, volume 7914, pp. 364–371, (SPIE2011). DOI:10.1117/12.873291.

22. F. Sidiroglou, A. Roberts, and G. Baxter. Contributed review: A review of the investigation of rare-earth dopant profiles in optical fibers, Rev. Sci. Instrum. **87** (2016). DOI:10.1063/1.4947066.

23. M. Vivona, J. Kim, and M. N. Zervas. Non-destructive characterization of rare-earth-doped optical fiber preforms, Opt. Lett. **43**, 4907 (2018). DOI:10.1364/OL.43.004907.

24. X. Chen, T. Yao, L. Huang, Y. An, H. Wu, Z. Pan, and P. Zhou. Functional fibers and functional fiber-based components for high-power lasers, Adv. Fiber Mater. **5**, 59 (2023). DOI:10.1007/s42765-022-00219-7.

25. M. J. Barber, P. C. Shardlow, P. Barua, J. K. Sahu, and W. A. Clarkson. Nested-ring doping for highly efficient 1907 nm short-wavelength cladding-pumped thulium fiber lasers, Opt. Lett. **45**, 5542 (2020). DOI:10.1364/OL.401228.

26. M. Grábner, B. Švejkarová, J. Aubrecht, J. Pokorný, P. Honzátko, and P. Peterka. Rise of amplified spontaneous emission in high-power thulium-doped fiber lasers and amplifiers due to self-heating, Opt. & Laser Technol. **180**, 111428 (2025). DOI:10.1016/j.optlastec.2024.111428.

27. M. Grábner, P. Peterka, and P. Honzátko. Formula for temperature distribution in multi-layer optical fibres for

high-power fibre lasers, Opto-Electronics Rev. **29**, 126 (2021). DOI:10.24425/opelre.2021.139482.

28. B. Jiříčková, M. Grábner, C. Jauregui, J. Aubrecht, O. Schreiber, and P. Peterka. Temperature-dependent cross section spectra for thulium-doped fiber lasers, Opt. Lett. **48**, 811 (2023). DOI:10.1364/OL.479313.

29. B. Jiříčková, R. Švejkar, M. Grábner, C. Jauregui, J. Aubrecht, O. Schreiber, and P. Peterka. Temperature-dependent emission cross-section spectra at 1.8 μm of the thulium-doped fibers cooled down to cryogenic temperatures, In *The European Conference on Lasers and Electro-Optics*, p. cj‗10‗6, (Optica Publishing Group2023). DOI:10.1109/CLEO/Europe-EQEC57999.2023.10232759.

30. M. Grábner, K. Nithyanandan, P. Peterka, P. Koška, A. A. Jasim, and P. Honzátko. Simulations of pump absorption in tandem-pumped octagon double-clad fibers, IEEE Photonics J. **13**, 1 (2021). DOI:10.1109/JPHOT.2021.3060857.